Article

Forward Scatter Radar for Air Surveillance: Characterizing the Target-Receiver Transition from Far-Field to Near-Field Regions

Marta Tecla Falconi *, Davide Comite, Alessandro Galli, Debora Pastina, Pierfrancesco Lombardo and Frank Silvio Marzano

Department of Information Engineering, Electronics and Telecommunications, Sapienza University of Rome, Via Eudossiana, 18, 00184 Rome, Italy; comite@diet.uniroma1.it (D.C.); galli@diet.uniroma1.it (A.G.); debora@infocom.uniroma1.it (D.P.); pierfrancesco.lombardo@uniroma1.it (P.L.); marzano@diet.uniroma1.it (F.S.M.)

* Correspondence: falconi@diet.uniroma1.it; Tel.: +39-06-4458-5678

Abstract: A generalized electromagnetic model is presented in order to predict the response of forward scatter radar (FSR) systems for air-target surveillance applications in both far-field and near-field conditions. The relevant scattering problem is tackled by developing the Helmholtz–Kirchhoff formula and Babinet's principle to express the scattered and the total fields in typical FSR configurations. To fix the distinctive features of this class of problems, our approach is applied here to metallic targets with canonical rectangular shapes illuminated by a plane wave, but the model can straightforwardly be used to account for more general scenarios. By exploiting suitable approximations, a simple analytical formulation is derived allowing us to efficiently describe the characteristics of the FSR response for a target transitioning with respect to the receiver from far-field to near-field regions. The effects of different target electrical sizes and detection distances on the received signal, as well as the impact of the trajectory of the moving object, are evaluated and discussed. All of the results are shown in terms of quantities normalized to the wavelength and can be generalized to different configurations once the carrier frequency of the FSR system is set. The range of validity of the proposed closed-form approach has been checked by means of numerical analyses, involving comparisons also with a customized implementation of a full-wave commercial CAD tool. The outcomes of this study can pave the way for significant extensions on the applicability of the FSR technique.

Keywords: forward scatter radar (FSR); low-signature air-target detection; radar cross-section (RCS); electromagnetic scattering modeling; numerical techniques

1. Introduction

The detection of objects with reduced radar cross-section (RCS) is one of the most challenging problems for air-target surveillance applications. Due to an ever-increasing diffusion of unmanned aerial vehicles (UAVs), in particular drones, air-traffic systems capable of providing reliable surveillance and avoiding violation of no-fly zones look highly desirable. Moreover, the traffic control of city airspace is crucial for population safety. UAVs are typical examples of low-signature targets that may result in being practically invisible to common monostatic or bistatic radar systems [1,2]. In general, objects having a small size and made of particular materials exhibit a reduced cross-section; this also happens to big-sized targets of special shapes having the capability of redirecting the electromagnetic (EM) waves in different directions with respect to the illuminating antenna.

Typical examples of UAVs showing a small size (about 1 m for the largest dimension) and reduced RCS are represented by remote-controlled drones, whose spread is exponentially increasing, particularly for remote video observation and for a wide class of security applications. On the other hand, military UAVs having a size of about 15–20 m are often designed with stealth technology, which typically consists of choosing appropriate shapes and covering layers with composite materials having high absorption coefficients [2].

The detection of these targets by ground-based conventional radars, using monostatic or bistatic configurations with bistatic angles significantly lower than 180°, may be very challenging and is a topic of increasing interest for the modern radar community [3]. Indeed, the signal scattered by the illuminated target and collected by the receiving antenna may result in being particularly weak due to the very low value of the RCS. In this context, radar systems based on the forward scatter (FS) phenomenon may offer the clear advantage of stronger scattered returns with respect to monostatic systems, as well as weaker dependence on the target material and composition [4].

The forward scatter radar (FSR) is a special class of radar systems characterized by a bistatic angle that approaches or reaches 180°, with targets crossing the transmitter-receiver baseline (BL) and following an arbitrary trajectory, as shown in the example of Figure 1a. Under certain conditions, this configuration has shown peculiar capabilities to enhance the detection of low-signature targets [5]. This is related to the RCS enhancement exhibited by the illuminated object: from a physical viewpoint, such an improvement is produced in the forward direction due to co-phase interference of the EM waves arising from the illuminated side of the object, which produces a field focused on the opposite direction with respect to the impinging wave [6,7]. Therefore, the FSR system is now considered a viable alternative with respect to 'conventional' radars, being able to theoretically provide a forward-scatter cross-section (FS-CS) several dB higher than the conventional backscatter RCS [5,8]. It is also noted that, in the frame of civil applications, the possibility to apply FSR systems as passive radar configurations with no power emission may result in being particularly effective [9–15].

(**a**)   (**b**)
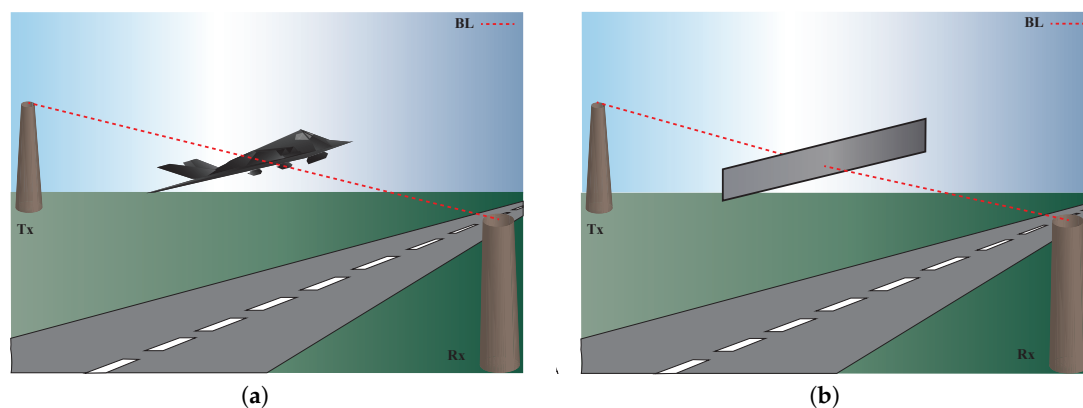
Figure 1. Typical forward scatter radar (FSR) scenario. (**a**) An air target crosses the baseline (BL) between transmitting (Tx) and receiving (Rx) antennas; (**b**) the same target is replaced by a two-dimensional (2D) rectangular metallic sheet approximating the illuminated object.

Different types of FSRs, both wide-band and narrow-band, have been analyzed so far, and simple models assuming far-field (FF) conditions have recently been proposed [16–18]. Nevertheless, a wider diffusion of the FSR technique especially for short-range applications would largely benefit from the availability of a comprehensive EM model of the involved scattering phenomenon, also valid in near-field (NF) conditions. In this frame, a straightforward approach has been proposed in [17] and used in [19–22], where the received signal is decomposed into a chirp-like waveform, which is the Doppler signature related to the motion, and an envelope pattern, which is in turn a function of the target shape and size. In any case, a fundamental assumption involving FF conditions has been considered so far to evaluate the signal collected by the receiver: this requires that the distance

between the transmitting (Tx) antenna and the target, as well as the distance between the target and the receiving (Rx) antenna are sufficiently large in terms of the involved wavelengths. In order to test the significant effects of near-field conditions on the forward scattered field and on the relevant chirp-like signature, a preliminary extension of this model has been proposed in [23,24].

Indeed, the signal collected in FSR configurations results in being particularly sensitive to the geometry of the considered scenario. In fact, the characteristic dimensions and location of the involved target with respect to the impinging wavelengths, along with the distance between the Tx-Rx antennas, determine the main features of the FS phenomenon characterizing the overall system. For these reasons, to accurately predict the received signal and allow for the design of optimal processing techniques [25], a more general and accurate EM modeling of the forward scattering phenomenon is extremely important and desirable.

In this context, the main goal of the present work consists of deriving and discussing a comprehensive EM model of the received FSR signal in more general conditions, which involve also important NF applications: the FS problem is formulated as a standard diffraction problem [26]; hence, the solution is developed by considering the Helmholtz–Kirchhoff formula [27] along with Babinet's principle [28,29]. An exact evaluation of the field in the 'shadow' region of the target is thus achieved under the physical-optics approximation [7], valid when the target dimension is large in terms of the operative wavelengths. In order to emphasize the essential features of the problem, we will refer to a plane wave impinging on a metallic canonical shape [30], and the specific effects of possible near-field conditions are considered on the collected signal, since in many applications, the Rx antenna could be located at a few wavelengths from the moving target. In particular, an efficient analytical formulation for the scattered and total fields is carried out, which is valid for Rx both in FF and NF conditions, considering a rectangular silhouette (see Figure 1b) under first-order approximation in the phase expansion. It is noted that a generalization to a complex object could be obtained by using Glaser's approach [5,31]. The solution of our scattering formulation is anyway achievable by numerically evaluating the diffraction integrals both for simple rectangular geometries and also for arbitrarily-shaped objects. The relevant analyses will consider here various scenarios for changing distances between the target and Rx and for variously-shaped and -sized objects following straight trajectories either perpendicular or at an angle with respect to the considered baseline [32]. Moreover, to further validate the proposed model, a full-wave solution has also been implemented based on state-of-the-art commercial EM CAD (computer-aided design) tools. As said, the NF effects are considered for the Rx antenna, and the approach is useful for many applications in which the Tx antenna is in FF with respect to the target. Due to reciprocity [28], by the collected response for a target-Rx configuration in NF, it is possible to derive the behavior in NF also for the target-Tx. It is finally worth noting that the proposed approach can be further generalized to the monitoring of wide ranges of airspace using a network of cooperating FSR sensors [33,34].

The paper is organized as follows. Methods are provided in Section 2, including a theoretical background, the geometry of the FSR system and the proposed analytical model valid also in near-field conditions. Results for both the NF and FF region are presented in Section 3 with full-wave validations through an ad hoc implementation of an EM CAD tool. The discussion in Section 4 emphasizes the role played by different geometrical parameters (distance, size and trajectory of the target) on the gathered signal. Conclusions follow in Section 5.

2. Methods

In this section, methods are presented to recall the fundamentals of the electromagnetic theory useful to frame our proposed model. After, the basic FSR geometry is described to insert the theory in a real contest and to present the numerical and analytical model.

2.1. Theoretical Background

The evaluation of the FSR signal collected by the Rx antenna can be modeled as a standard diffraction problem. When an EM wave impinges on an obstacle, following the physical theory of diffraction (PTD), the scattered (diffracted) field can be viewed as generated by surface sources induced on the object by the incident wave [26,27,30]. In the forward direction, if the target dimensions are larger than the operating wavelength λ (a time-harmonic regime is assumed with $\lambda = c/f$, where f is the carrier frequency and c the speed of light in vacuum), a shadow region is generated [7]. Beyond this zone, directly opposite the object, there is a forward region in which the fields add up roughly in phase, generally producing a strong radiation peak responsible for the enhanced RCS. The pattern of this forward radiation can be related to the scattered pattern due to an aperture on a screen having the same silhouette of the object. The physical explanation of the phenomenon can be derived through the well-known Babinet's principle (BP) [27–29]; by applying the equivalence theorem, if the target is replaced with its silhouette, the induced currents on the target must be equal to the surface current on an infinite plane [7,35]. Hence, thanks to the shadow-contour theorem [6,7,16], which states that different objects with identical shadow boundaries generate identical shadow (forward) radiation, this concept can be further generalized to three-dimensional (3D) targets. This assumption can significantly facilitate the approximate estimation of the scattering generated by a wide class of objects. As a reference case, we consider in the following two-dimensional (2D) rectangular metallic targets, and we focus the attention on the characterization of the transition between far-field and near-field regions.

The total electric field due to a surface field distribution on the aperture A of a metallic screen (PEC (perfect electric conductor) is assumed), whose normal direction is n' (see, e.g., Figure 2a), can be obtained through the well-known Helmholtz–Kirchhoff formula [27]:
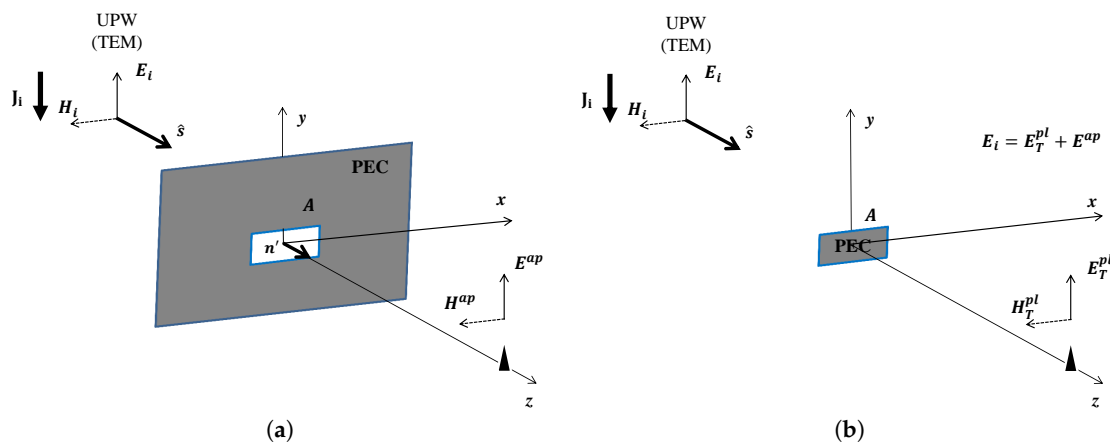
Figure 2. Formulation for the considered scattering problem: (**a**) Canonical example of planar aperture A on a screen illuminated by an incident field, represented here as a uniform plane wave (UPW), that is transverse electromagnetic (TEM). The PEC boundary conditions hold on the metallic screen. (**b**) According to duality and Babinet's principles, a complementary metal shape illuminated by the field as in (a) is represented: this is the case of specific interest for typical FSR applications. The field scattered by the metallic target is thus expressed in terms of the total field in the absence of any obstacle and of the field generated by the equivalent aperture (see the related formulas with the quantities defined in the text).

$$E^{ap}(\mathbf{r}) = \int_A \left(E(\mathbf{r}') \frac{\partial G(\mathbf{r}, \mathbf{r}')}{\partial n'} - G(\mathbf{r}, \mathbf{r}') \frac{\partial E(\mathbf{r}')}{\partial n'} \right) dA' \tag{1}$$

$E^{ap}(\mathbf{r})$ being the scalar electric field at any observation point $\mathbf{r}$ as a function of the total field $E(\mathbf{r}')$ and its normal derivative on the equivalent source points $\mathbf{r}'$ of the aperture A (where the superscript 'ap' is the abbreviation of 'aperture'); $G(\mathbf{r}, \mathbf{r}')$ represents the scalar Green's function of the problem. As is

well known, according to the uniqueness theorem, it is not necessary to specify both $E(\mathbf{r}')$ and its derivative with respect to the normal unit vector; thus, Equation (1) can be simplified [27]. The exact evaluation of the field on an aperture requires the solution of a typical boundary value problem. As a first approximation, the field at any point on the aperture can be assumed as the incident field on the tangent plane to the aperture. This approximation is well known as tangent approximation in optics, equivalent in electromagnetics to the physical optics or Kirchhoff approximation, and typically requires a maximum aperture size D large in terms of the considered wavelength ($D \geq \lambda$). By reasonably assuming the illumination of a linearly-polarized uniform (homogeneous) plane wave (*UPW*), that is transverse electromagnetic (*TEM*) having wavenumber $k = 2\pi f / c = \omega / c$ (ω being the angular frequency) and replacing in Equation (1) the incident field on the object, we have:

$$E(\mathbf{r}') = E_i(\mathbf{r}') = E_0 e^{-jk\hat{\mathbf{s}}\cdot\mathbf{r}'} \tag{2}$$

E_0 being a complex amplitude taking into account also the initial phase and $\hat{\mathbf{s}}$ the unit vector defining the UPW propagation direction. By exploiting Babinet's and the duality principles [27], for our FSR applications, we can relate the canonical scattering problem due to a planar aperture on a screen (a) to that of a complementary metal PEC shape illuminated by the same source, as in Figure 2b. We can therefore write the total electric field in the forward direction of a target A on a plane surface as follows:

$$E_T^{pl}(\mathbf{r}) = E_i(\mathbf{r}) - E^{ap}(\mathbf{r}) \tag{3}$$

$E^{ap}(\mathbf{r})$ being the aperture field obtained from Equation (1) along with the choice of Equation (2), and $E_T^{pl}(\mathbf{r})$ the total field radiated by the metal object (i.e., the PEC surface of area A as in Figure 2b, where the superscript 'pl' is the abbreviation for 'plate'): these fields are related to the overall field $E_i(\mathbf{r})$ in the absence of any obstacle.

In more general cases, from Equation (3), we can reach the following integral expression in terms of the free-space Green's function $G(\mathbf{r}, \mathbf{r}') = e^{-jk|\mathbf{r}-\mathbf{r}'|}/4\pi|\mathbf{r}-\mathbf{r}'|$ [27]:

$$E_T^{pl}(\mathbf{r}) \quad = E_i(\mathbf{r}) - \int_A \left[E_i(\mathbf{r}') \left(jk + \frac{1}{|\mathbf{r}-\mathbf{r}'|} \right) \frac{z}{|\mathbf{r}-\mathbf{r}'|} - \frac{\partial E_i(\mathbf{r}')}{\partial n'} \right] \frac{e^{-jk|\mathbf{r}-\mathbf{r}'|}}{4\pi|\mathbf{r}-\mathbf{r}'|} \, dA' \tag{4}$$

This represents a generalized expression for the total field scattered by a plane metallic object A illuminated by an incident field E_i. According to the uniqueness theorem, if the field $E_i(\mathbf{r}')$ (or $\frac{\partial E_i(\mathbf{r}')}{\partial n'}$) is known on the surface, the field should be uniquely determined everywhere outside the surface [27]; hence, from Equation (4), we can finally reach the reference expression:

$$E_T^{pl}(\mathbf{r}) \quad = E_0 \left(e^{-jk\hat{\mathbf{s}}\cdot\mathbf{r}} - \frac{1}{2\pi} \int_A e^{-jk\hat{\mathbf{s}}\cdot\mathbf{r}'} \left(jk + \frac{1}{|\mathbf{r}-\mathbf{r}'|} \right) \frac{z}{|\mathbf{r}-\mathbf{r}'|} \frac{e^{-jk|\mathbf{r}-\mathbf{r}'|}}{|\mathbf{r}-\mathbf{r}'|} \, dA' \right) \tag{5}$$

This is an integral relation describing in our cases of interest the radiation produced by a metallic target A crossing the baseline between Tx and Rx: the source is assumed in FF with respect to the illuminated object, while the receiver is located at an arbitrary distance (FF or NF) from the scatterer. From Equation (5), we can easily derive also the scattered field (labeled with subscript S) from the plane section A illuminated by the incident field E_i as:

$$E_S^{pl}(\mathbf{r}) \quad = E_T^{pl}(\mathbf{r}) - E_i(\mathbf{r}) = -E^{ap}(\mathbf{r}) \tag{6}$$

This expression highlights for FSR the relation between the scattered field from an obstacle A and the well-known formula of the field produced by an equivalent planar aperture on a screen. Overall, Equations (5) and (6) represent the basic step toward the derivation of a simple analytical expression for the electric field re-irradiated by a target and collected by the Rx antenna in general FSR scenarios.

2.2. Electromagnetic Modeling

The basic FSR geometry is sketched in Figure 3, where the moving target is illuminated by a source located in the far-field while crossing a baseline (BL). The moving target has an arbitrary linear trajectory, between x_i and x_f, in the xz plane and described by a tilt angle ψ and a horizontal angle α_h. The signal propagating along the direct path of the BL between Tx and Rx antennas is gradually reduced by the target shadow, which is generated as the object reaches its central position (i.e., for $\alpha_h = 0°$), where it results in being exactly interposed between the antennas.
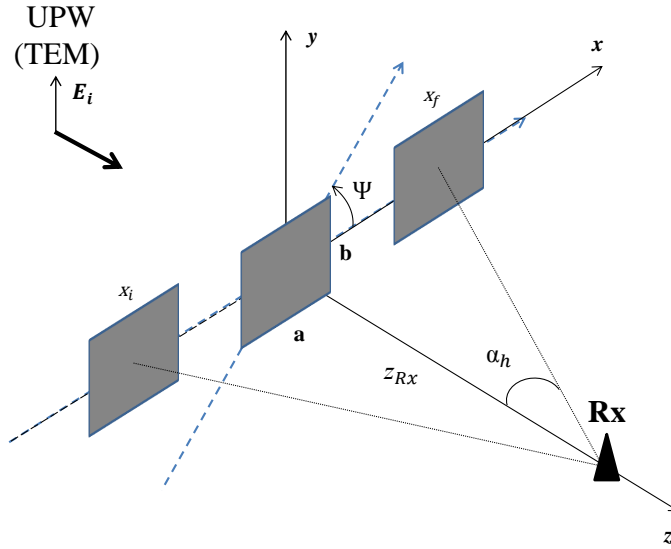
Figure 3. Simulated scenario and frame for the considered FSR analysis. The metallic target of the rectangular shape crosses the baseline moving from x_i to x_f with a uniform linear motion (constant velocity or zero acceleration).

We consider specifically a rectangular target having dimensions a and b with respect to the x and y axes, respectively. The fundamental geometrical parameter z_{RX} is the distance from the Rx antenna to the center of the target shape when the BL is crossed (that is the origin of the coordinate system of Figure 3). By transmitting a continuous wave (CW) at angular frequency ω, the received total field due to the target plate can be expressed from Equation (5):

$$E_T^{pl}(\mathbf{r}, \omega) \quad = E_0 \left(e^{-jk z_{Rx}} - \frac{1}{2\pi} \int_A \left(jk + \frac{1}{R} \right) \frac{z_{Rx}}{R^2} e^{-jkR} \, dA' \right) \tag{7}$$

where:

$$R = |\mathbf{r} - \mathbf{r}'| = \sqrt{(x_t - x')^2 + (y_t - y')^2 + (z_{Rx})^2} = \lambda \tilde{R} \tag{8}$$

and:

$$\tilde{R} = \sqrt{(\tilde{x}_t - \tilde{x}')^2 + (\tilde{y}_t - \tilde{y}')^2 + (\tilde{z}_{Rx})^2} \tag{9}$$

R being the distance between the observation point $\mathbf{r}$ (where the Rx antenna is located) and the arbitrary source point $\mathbf{r}'$ of the target shape; x_t and y_t are the coordinates of the target center on the $z = 0$ plane at each instant, and x' and y' are the target local coordinates referring to its center. In order to generalize the previous expressions, we define $\tilde{R}$ in Equation (9) as the distance R normalized with respect to the wavelength λ. The rectangular coordinates are normalized as follows: $\tilde{x}_t = x_t/\lambda$, $\tilde{y}_t = y_t/\lambda$, $\tilde{x}' = x'/\lambda$, $\tilde{y}' = y'/\lambda$ and $\tilde{z}_{Rx} = z_{Rx}/\lambda$ (i.e., all of the quantities with the 'tilde' are normalized with respect to the wavelength). By introducing the normalized coordinates and the normalized wavenumber

$\tilde{k} = k\lambda = 2\pi$, Equation (7) becomes independent of the angular frequency ω; we can therefore write the expression of the received total field as follows:

$$E_T^{pl}(\tilde{\mathbf{r}}) \quad = E_0 \left(e^{-j\tilde{k}\tilde{z}_{Rx}} - \frac{1}{2\pi} \int_{\tilde{A}} \left(j\tilde{k} + \frac{1}{\tilde{R}} \right) \frac{\tilde{z}_{Rx}}{\tilde{R}^2} e^{-j\tilde{k}\tilde{R}} \, d\tilde{A}' \right) \tag{10}$$

the integral evaluated on the surface of normalized area being $\tilde{A} = A/\lambda^2$. These are reference expressions for our model and allow one to numerically evaluate the FSR scattering effects for arbitrary angular frequencies and arbitrary metallic targets, both in FF and NF conditions.

We first aim at achieving a simple but accurate closed-form solution of the considered integral in Equation (10), also accounting for near-field conditions that may occur between the illuminated rectangular-shaped target and receiver.

We exploit two canonical approximations: (i) paraxial approximation, valid in general when the longitudinal distance of a point-like target from the Rx can be considered greater than the transverse distance; (ii) first-order Taylor's approximation on the phase expansion of the re-irradiated signal given by Equation (10). Hence, Equation (9) can be written as follows:

$$\tilde{R} \approx \tilde{z}_{Rx} + \frac{(\tilde{x}_t - \tilde{x}')^2 + (\tilde{y}_t - \tilde{y}')^2}{2\tilde{z}_{Rx}} \tag{11}$$

On this basis, a closed-form solution of the integral in Equation (10) can be obtained for a rectangular-shaped target with normalized sizes $\tilde{a} = a/\lambda$ and $\tilde{b} = b/\lambda$, with respect to the x and y axis.

After some algebra (the relevant details are reported in the Appendix A), Equation (10) reduces to:

$$E_T^{pl}(\tilde{\mathbf{r}}) = E_0 e^{-j\tilde{k}\tilde{z}_{Rx}} \left(1 - \frac{1}{2\tilde{k}} \frac{\tilde{z}_{Rx}^2}{\tilde{R}_0^2} \left(j\tilde{k} + \frac{1}{\tilde{R}_0} \right) \right)$$

$$[-C(p^-) + jS(p^-) + C(p^+) - jS(p^+)][-C(q^-) + jS(q^-) + C(q^+) - jS(q^+)] \tag{12}$$

where $\tilde{R}_0 = \sqrt{\tilde{x}_t^2 + \tilde{y}_t^2 + \tilde{z}_{Rx}^2}$, C and S are the cosine and sine Fresnel integrals [27], and:

$$p^\pm \quad = \left(\tilde{x}_t \pm \frac{\tilde{a}}{2} \right) \sqrt{\frac{2}{\tilde{z}_{Rx}}} \tag{13}$$

$$q^\pm \quad = \left(\tilde{y}_t \pm \frac{\tilde{b}}{2} \right) \sqrt{\frac{2}{\tilde{z}_{Rx}}} \tag{14}$$

Equation (12) provides a straightforward analytical expression for the evaluation of the FSR signal generated by canonical shapes both in far-field (Fraunhofer) and near-field (Fresnel) configurations (Figure 3). By applying again the paraxial approximation, along with a first-order expansion for the phase and neglecting the quadratic term related to the size of the target, we can write:

$$\tilde{R} \quad \approx \tilde{z}_{Rx} + \frac{\tilde{x}_t^2 + \tilde{y}_t^2}{2\tilde{z}_{Rx}} - \frac{\tilde{x}_t \tilde{x}' + \tilde{y}_t \tilde{y}'}{\tilde{z}_{Rx}} \tag{15}$$

Hence, by assuming a distance z_{Rx} much larger than the target size and the wavelength ($\tilde{z}_{Rx} > 1$), the well-known Fraunhofer formula is obtained:

$$E_T^{pl}(\tilde{\mathbf{r}}) = E_0 \left(e^{-j\tilde{k}\tilde{z}_{Rx}} - \frac{1}{2\pi} \frac{\tilde{z}_{Rx}}{\tilde{R}_0^2} \left(j\tilde{k} + \frac{1}{\tilde{R}_0} \right) e^{-j\tilde{k}\left(\tilde{z}_{Rx} + \frac{\tilde{x}_t^2 + \tilde{y}_t^2}{2\tilde{z}_{Rx}} \right)} \tilde{a}\tilde{b} \operatorname{sinc}\left(\frac{\tilde{x}_t \tilde{a}}{\tilde{z}_R} \right) \operatorname{sinc}\left(\frac{\tilde{y}_t \tilde{b}}{\tilde{z}_R} \right) \right) \tag{16}$$

It is interesting to note that Equation (16) correctly models the FS phenomenon in the far-field (Fraunhofer) region by means of Babinet's principle, showing the diffraction pattern, but in general, it fails in predicting well a neat shadow effect, which is instead present in the near-field case. Indeed, by

neglecting the quadratic phase term, we prevent the creation of the shadow effect that is responsible for the persistent destructive interference between the direct and the scattered field. In other words, the Fraunhofer approximation gives a field radiated by a target that can be derived from elementary surfaces radiating in a parallel fashion; as a result, the interference phenomenon does not generate a shadow region. Such observations are in full agreement with the results in [17], where it is shown that a model for the FSR in the far-field region can be obtained by modulating the signal re-irradiated by the target in the far zone with the Doppler signature produced by a moving point-like scatterer.

3. Results

In this section, numerical results are provided to test the proposed model for the FSR problem. A target of fixed dimensions has been chosen to evaluate the proposed analytical model, both in the FF and NF conditions. Numerical validations are provided. The sensitivity of the model proposed in the previous section with respect to the approximations reported in Equations (11) and (15) is analyzed.

3.1. Far-Field and Near-Field Forward Scattering

A first result for a square object having dimensions $\tilde{a} = \tilde{b} = 3$ illuminated through a plane wave having carrier frequency f (related to $\lambda = c/f$) and a linear-polarized (e.g., along y) electric field with the amplitude equal to 1 V/m is considered (see, e.g., Figure 3). In Figure 4, the field collected by the receiving antenna placed at an 'FF' distance $\tilde{z}_{Rx} = 200$ is reported (the typical Fraunhofer distance $R_F = 2D^2/\lambda = 4a^2/\lambda$ is equal to 36 in this case). The amplitude (A) and phase (Φ) of both 'scattered' field (i.e., related to the FS-CS of the illuminated target, 'S' subscripts in Figure 4) and 'total' field (i.e., made by the interference between impinging and re-irradiated waves, 'T' subscripts in Figure 4) are displayed on a double axis, representing the target movement along x and the relevant spanned horizontal angle α_h. The effect of the interference between the direct and the re-irradiated field is clearly visible by comparing the two contributions. It is noted that the amplitude value of the total field collected when the object is in $x = 0$ is equal to 1 V/m, whereas the scattered field is 0.045 V/m. Indeed, the field re-irradiated by the target is a spherical wave that decays for increasing distances; when the impinging plane wave is also considered, beyond the object (acting as a shield), it goes on propagating up to the receiving antenna without undertaking a significant attenuation, and a field equal to 1 V/m is detected by the receiving antenna modeled as a short electric dipole. In addition, as expected since the target is in movement, the scattered field shows a parabolic variation of the phase (see Figure 4b,e for the wrapped and unwrapped case, respectively), whereas the phase of the total field is affected by the interference phenomenon, which represents indeed the peculiarity of this system. It is worth noting that in Figure 4b,e, the phase obtained by implementing the Fraunhofer formula in (16) is reported: a parabolic phase variation not presenting any oscillation has been obtained, confirming the inherent point-like nature of the scattering generated by the target. We emphasize that, as expected for these results obtained in the Fraunhofer region, the validity of our general analytical model ('AM'), based on Equation (12), is very good with respect to both the approximate FF model ('AM(FF)'), based on Equation (16), and also to the numerical model ('NM'), based on the computation of Equation (10). Moreover, all of the results presented here have independently been validated by means of an ad hoc implementation on a commercial software (FEKO) [36], which performs a full-wave EM solution based on the method of moments: the same scenarios are considered, with the source modeled as a linear polarized plane wave having the same amplitude and initial phase. All of the results generated on the CAD full-wave model are labeled with 'FW'. Overall, an excellent agreement has been obtained, confirming the accuracy of the proposed formulation. In Figure 5, the field collected in a near-field configuration is analyzed, by considering the same FSR system, but placing the Rx antenna at $\tilde{z}_{Rx} = 10$ from the target (Fresnel region). The peak value of the amplitude of the scattered field is equal here to 0.85 V/m, resulting in being less attenuated with respect to the field in Figure 4a; this is coherent with the shorter distance between the re-irradiating object and the receiving short dipole. In this case, even though the target is tracing the same trajectory under the same angle-of-view (i.e, equal to 40° for

both FF and NF case), the length of the trajectory decreases (from about 70 for the FF case to 3.5 for the NF); hence, the phase variation of the scattered field changes accordingly. The same effect can be observed on both the phase and amplitude of the total field. Furthermore, in this case, an excellent agreement has been obtained with the full-wave CAD simulations, confirming the accuracy of the proposed analytical model also for the NF cases. In Table 1, we characterize the results previously presented for two typical configurations, i.e., small and large UAVs (1 m and 20 m).
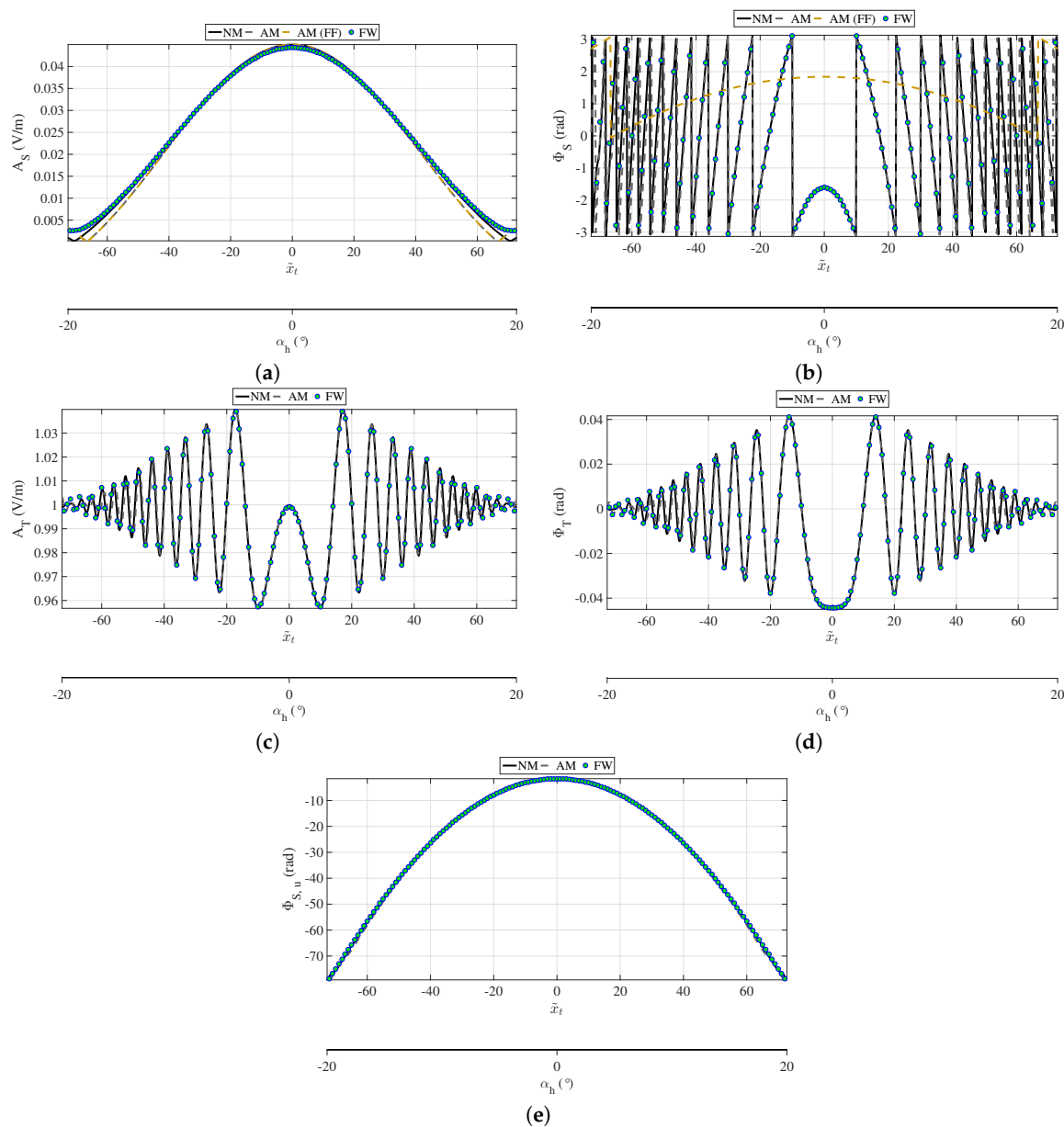
Figure 4. FSR scattered (subscripts 'S') and total (subscripts 'T') fields collected by the receiving antenna for a square metallic object horizontally moving in the far-field with respect to the Rx antenna having a size of $\tilde{a} = \tilde{b} = 3$. The distance object-Rx antenna $\tilde{z}_{Rx} = 200$ for a generalized frequency f. The source is assumed in the far-field and modeled in terms of a plane wave linearly polarized along the y-direction, having amplitude equal to 1 V/m and zero initial phase. Different analytical and numerical methods have been used and compared. Legend: NM = numerical solution of the integral (Equation (7)), AM = analytical solution (Equation (12)), AM(FF) = analytical solution with FF approximation (Equation (16)), FW = full-wave CAD solution. (**a**) Amplitude (S); (**b**) phase (S); (**c**) amplitude (T); (**d**) phase (T); (**e**) unwrapped phase (S).
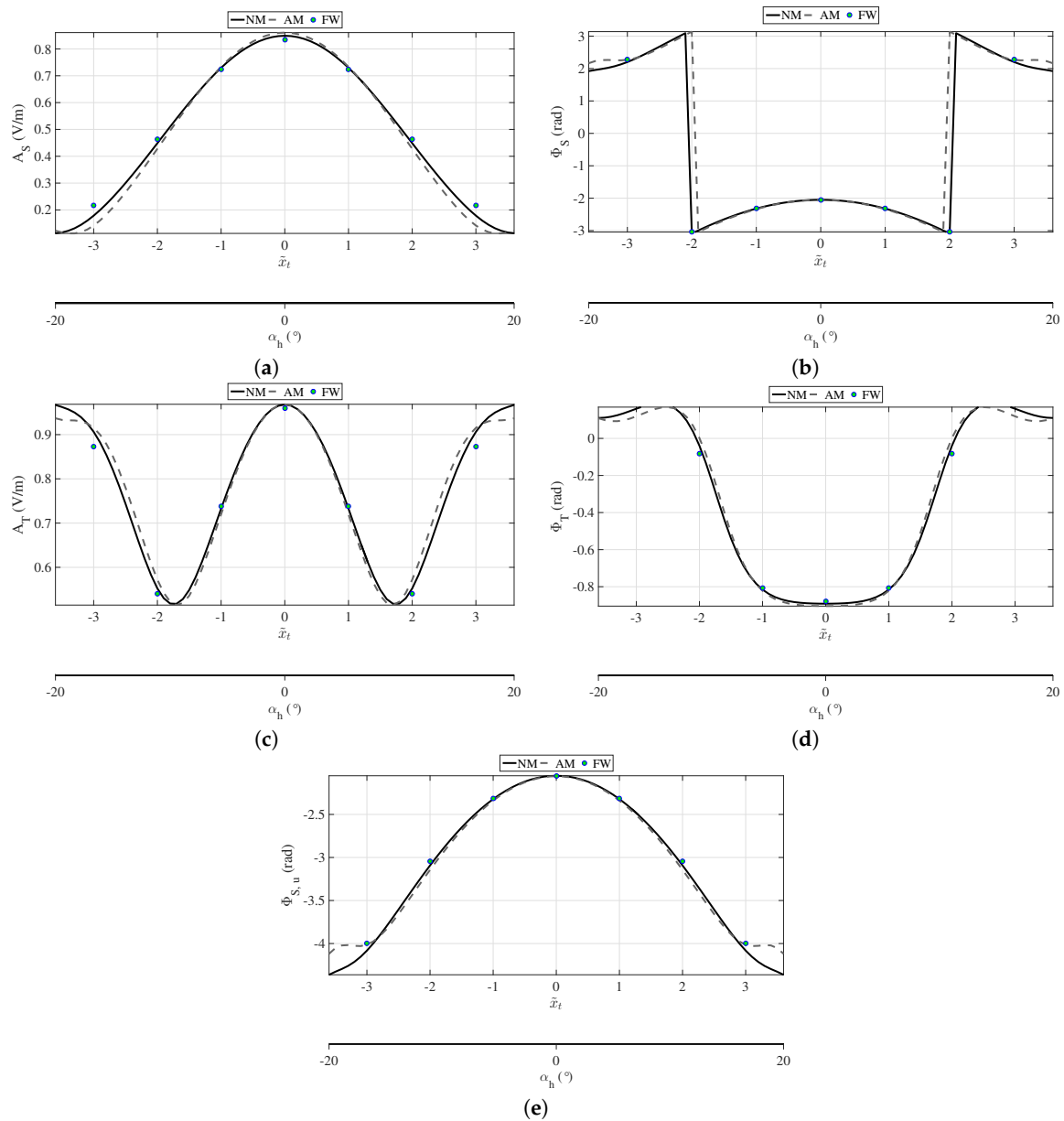
Figure 5. As in Figure 4, for a near-field case with $\tilde{z}_{Rx} = 10$. (**a**) Amplitude (S); (**b**) phase (S); (**c**) amplitude (T); (**d**) phase (T); (**e**) unwrapped phase (S).

Table 1. Parameters of the results.

$a = b$ (m)	λ (m)	$frequency$ (MHz)	z_{Rx} (m)		x_t (m)	
			10λ	200λ	10λ	200λ
1	0.33	900	3.33	66.66	1.1667	23.33
20	6.66	45	66.66	1333.33	23.33	466.66

3.2. Model Sensitivity

The phase error $\Delta\Phi$ obtained neglecting the second-order quadratic term of the series expansion of Equation (15) can be written as:

$$\Delta\Phi = \tilde{k}\frac{(\tilde{a}/2)^2 + (\tilde{b}/2)^2}{2\tilde{z}_{Rx}} \tag{17}$$

For a square object and error phase equal to $\pi/8$, the well-known Fraunhofer far-field distance formula can be obtained (i.e., $z_{Rx,FF} > 2D^2/\lambda$). In the same way, the phase error obtained from Equation (11) (first-order expansion) can be written as:

$$\Delta\Phi = \quad \tilde{k}\frac{1}{8}\left[\frac{(\tilde{x}_t - \tilde{b}/2)^4 + (\tilde{y}_t - \tilde{a}/2)^4}{(\tilde{z}_{Rx})^3} + 2\frac{(\tilde{x}_t - \tilde{b}/2)^2(\tilde{y}_t - \tilde{a}/2)^2}{(\tilde{z}_{Rx})^3}\right] \tag{18}$$

Equation (18) represents the sensitivity formula for the analytical model proposed by (12). In Figure 6a, a two-dimensional representation of the formula in Equation (18) is shown for a square target with a variable size ($\tilde{a} = \tilde{b}$) and Rx-distance ($\tilde{z}_{Rx}$). The result is obtained replacing the terms related to the movement $\tilde{x}_t$ and $\tilde{y}_t$ with the value corresponding to a horizontal angle of $20°$. We note two regions at the top-right and bottom-left in which the phase error is very high: these correspond to a small Rx-distance and a big target, and to a big Rx-distance and a small target. These two regions are better highlighted in Figure 6b obtained by applying a threshold to the phase error in Figure 6a: such a threshold has been set to $\pi/8$, which is reasonable for radar applications. The sensitivity model expresses by Equation (18) is very useful to set up, once having fixed the wavelength and the horizontal angle a_h, the operational parameters such as the Rx-distance and the dimension of the target in order to have a defined accuracy on the phase approximation.
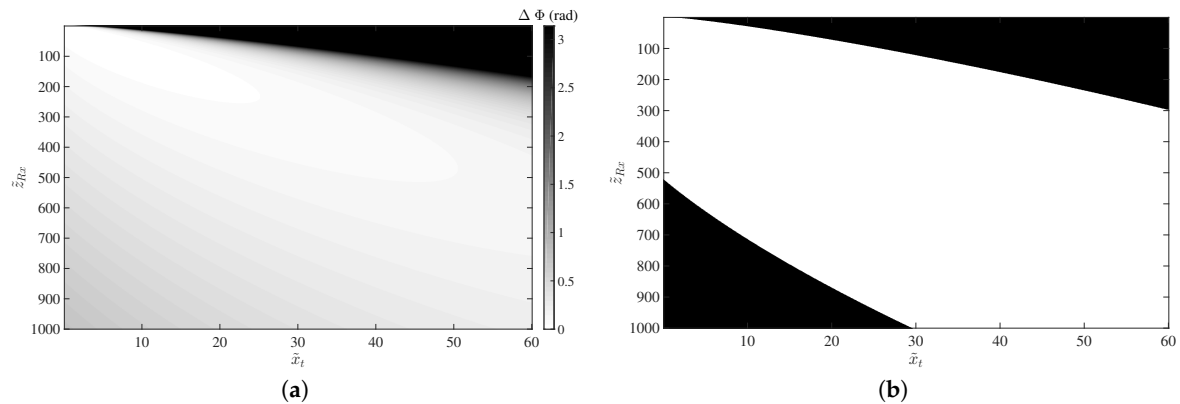
Figure 6. Evaluation of phase errors. (**a**) Maps of the phase error from Equation (18) for a horizontal angle ($a_h = 20°$). (**b**) Map of the area, where the phase error does not exceed $\pi/8$ (i.e., threshold $\pi/8$ applied to the data of case (a)). (a) Phase error maps; (b) validity maps under the threshold of $\pi/8$.

4. Discussion

In this section, we illustrate and discuss in more detail the original scattering features of an FSR system when the transition from FF to NF regions occurs; the effects of the target electrical dimensions on the received signal are evaluated; also, trajectories describing a certain angle with respect to the baseline are considered.

4.1. Transition from Far-Field to Near-Field

In Figure 7, the plane wave propagating along the BL direction z, having the electric field linearly polarized, e.g., along y, impinges on a square target when it traces a certain number of rectilinear trajectories sweeping from the FF to NF regions (i.e., by considering different values for z_{Rx}). The choice of a simple square shape, characterized by just one geometrical parameter ($a = b$), allows us to clearly emphasize the distinctive features of the scattering problem both in the FF and NF conditions.
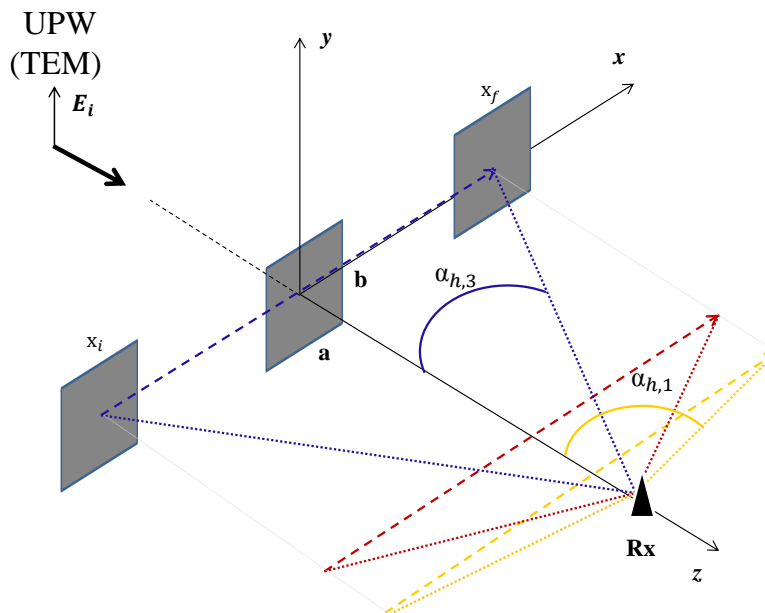
Figure 7. Simulated FSR scenario for different Rx-target distances: $\tilde{z}_{Rx_1} = 10$, $\tilde{z}_{Rx_2} = 30$, $\tilde{z}_{Rx_3} = 100$. The target is here a square metallic object having a side of $\tilde{a} = \tilde{b} = 3$ illuminated by CW having frequency f. Each distance generates a different angle-of-view from Rx, ranging from NF to FF ($\tilde{z}_{RX_1}$ to $\tilde{z}_{RX_3}$), i.e., $\alpha_{h,1} = 74°$, $\alpha_{h,2} = 49.4°$ and $\alpha_{h,3} = 19.3°$ (plot not to scale).

In Figure 8, the total and scattered field vs. x for a square object having side $\tilde{a} = \tilde{b} = 3$ crossing the baseline at different distances with respect to the receiver, from 10–100, is presented. The signal at the receiver is evaluated through the analytical closed-form model proposed in the previous sections (AM, solid lines). We assume that the target follows a linear horizontal trajectory along x between $\tilde{x}_i = -35$ and $\tilde{x}_f = 35$ and is moving with a uniform velocity spanning an angle of view α_h on the xz plane that is a function of the distance from the Rx antenna (see Figure 7). By selecting a fixed value for the length of the trajectory, α_h obviously results in being wider for shorter distances. In the results of Figure 8, for the normalized Rx-target distances $\tilde{z}_{Rx}$, we show 10 (yellow curves), 30 (red curves) and 100 (blue curves), thus considering both FF and NF operation conditions.

In Figure 8a–c, the scattered field is reported as a function of x: in particular, the amplitude A_S is shown in Figure 8a; in Figure 8b, we display the values of the unwrapped phase $\Phi_{S,u}$, and in Figure 8c, we plot the phase differences of the first-order approximations with respect to the correct numerical value, according to the considerations previously presented in Section 3.2. Comparisons between our analytical formulation (solid lines) and numerical full-wave CAD results (dots) are also provided.
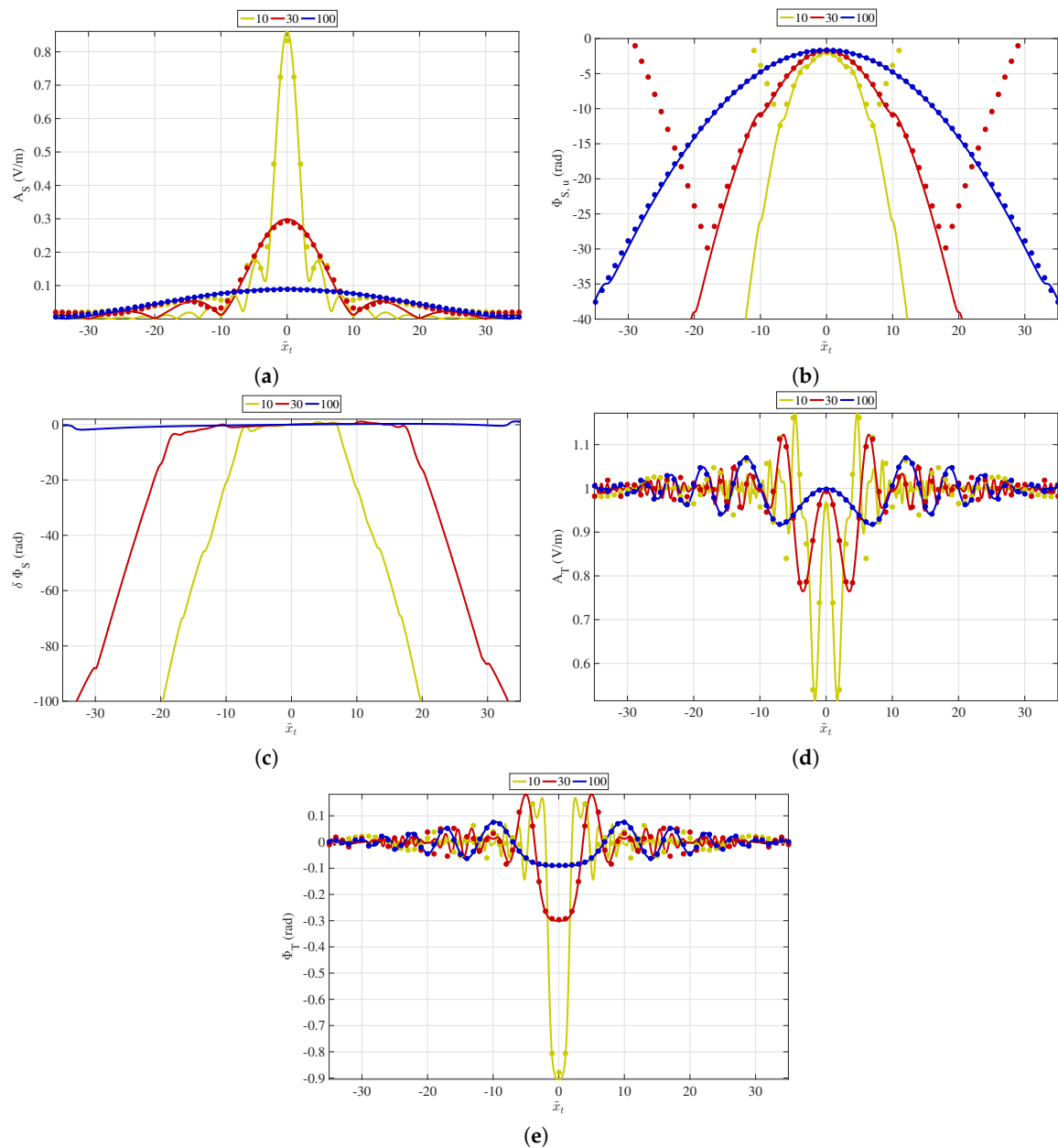
Figure 8. Scattered (subscripts 'S') and total (subscripts 'T') signals collected by the receiving antenna as the target moves along the *x*-direction (see Figure 7), for three different NF/FF distances, equal to 10 (yellow curves), 30 (red curves) and 100 (blue curves), where the solid lines refer to our analytical approach and dots to numerical CAD results. (**a**) Scattered amplitude; (**b**) unwrapped scattered phase; (**c**) phase difference between first-order approximation and numerical evaluation; (**d**) amplitude of the total received signal; (**e**) phase of the total received signal. Solid lines: AM; dots: FW.

As expected, the amplitude of the field scattered by the object (which acts as a re-irradiating element) is particularly sensitive to the distance $\tilde{z}_{Rx}$. This is coherent with the fact that, when we are no longer in FF conditions, the re-irradiated field can be viewed as a spherical wave whose power can decrease in a more complex way than $1/\tilde{z}_{Rx}^2$. The behavior of the beamwidth may result in being less predictable and should be interpreted by taking into account the relevant angle-of-view and the movement of the target; indeed, by moving farther from the Rx antenna, the angle of view decreases while covering the same distance along the *x* axis, and the object generates a re-irradiation that appears less variable. At the same time, even though when the FF is approached, the directivity of the object

generally increases and becomes independent of $\tilde{z}_{Rx}$ (and dependent just on θ and ϕ in the relevant spherical coordinate system): in fact, when the object is farther (i.e., $\tilde{z}_{Rx}$ is larger), it re-irradiates almost inside the main lobe of the radiation pattern, and consequently, the field at the receiving point results in being less variable (see, e.g., the blue curve in Figure 8a). The well-known far field concepts of directivity can be generalized in the near field, where this definition become dependent on the target/Rx distance [24]. The phase of the scattered field has a typical chirp-like behavior, where the phase oscillations along the distance are related to the well-known Doppler effect. Indeed, the unwrapped phase of the scattered signal, shown in Figure 8b, results in the expected parabolic trend. In Figure 8d,e, the values of the amplitude and phase of the total received signal, respectively, are presented. The effect of the interference between direct and re-irradiated waves confirms the expected FS phenomenon. In fact, the magnitude of the total field is oscillating around 1 V/m, and a fast variation is observed in the central part for reduced distances, due to strong variations of the field re-irradiated when the object is moving closer to the receiver. This aspect could result in being counter-intuitive and represents indeed an original feature of the FS phenomenon. As concerns the phase, going from the FF case up to the NF, the chirp-like nature of the signal is progressively lost.

As said, all of our results have been validated through the full-wave commercial code FEKO (all of the dotted data in Figure 8): it results in an excellent agreement obtained for the amplitude of both scattered and total fields (Figure 8a,d, respectively). It is interesting to note that the proposed model fails at predicting the phase of the field re-irradiated outside the central region, as clearly shown in Figure 8b,c: this is due to the truncated first-order expansion introduced to obtain the closed-form expression in (16), and it results in being manifestly worse when the target gets closer to the receiver (i.e., when $\tilde{a}$ is comparable to $\tilde{z}_{Rx}$ and we are no longer in FF conditions). In this case, to better approximate the phase behavior, more terms of the series expansion are needed, preventing the possibility to obtain a closed-form expression. Equation (18) is proposed to set up the limitations for our model.

4.2. Effect of the Target Size

In order to analyze the effects of the target size on the FSR signal, we consider here two different shapes, i.e., the square and the rectangle, each one having three different dimensions, as shown in Figure 9. In this case, we fix $\tilde{z}_{Rx} = 50$, with a correspondent overall angle-of-view equal to $70°$; all of the other parameters describing the trajectory and the FSR system remain unchanged, with the target still illuminated by a linear-polarized plane wave as in Figure 7.
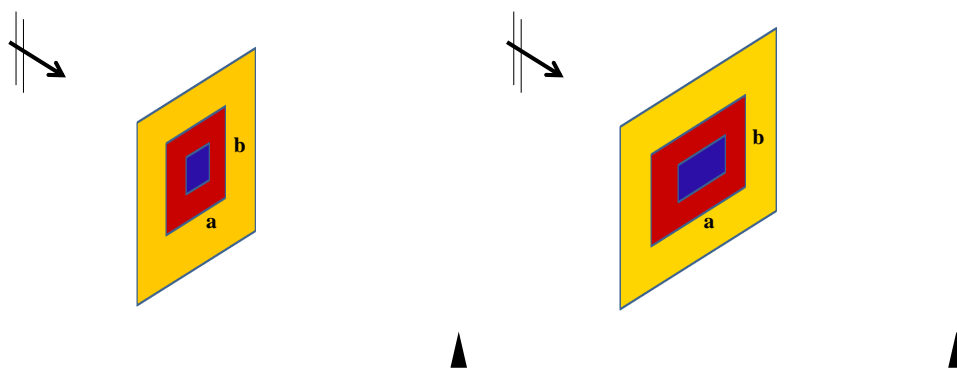
Figure 9. Simulated FSR scenario to investigate the effects of the target dimension and shape. Three different square (**left**) and rectangular (**right**) metallic plates are considered. Squares size along *x-y*: 1 (blue), 3 (red), 4 (yellow); rectangular size along *x-y*: 2×1 (blue), 6×3 (red), 8×4 (yellow).

In Figures 10 and 11, the scattered and the total fields are shown for increasing dimensions of the target profile, for a square and a rectangular shape, respectively: for the square side (Figure 10), it is $\tilde{a} = \tilde{b} = 1$ (blue), 3 (red) and 4 (yellow); for the rectangle (Figure 11), the same choices refer to the minor side $\tilde{b}$ along $\tilde{y}$, the major side being $\tilde{a} = 2\tilde{b}$ along x (see Figure 9). Again, our closed-form results (solid lines) are compared to full-wave CAD (dots).
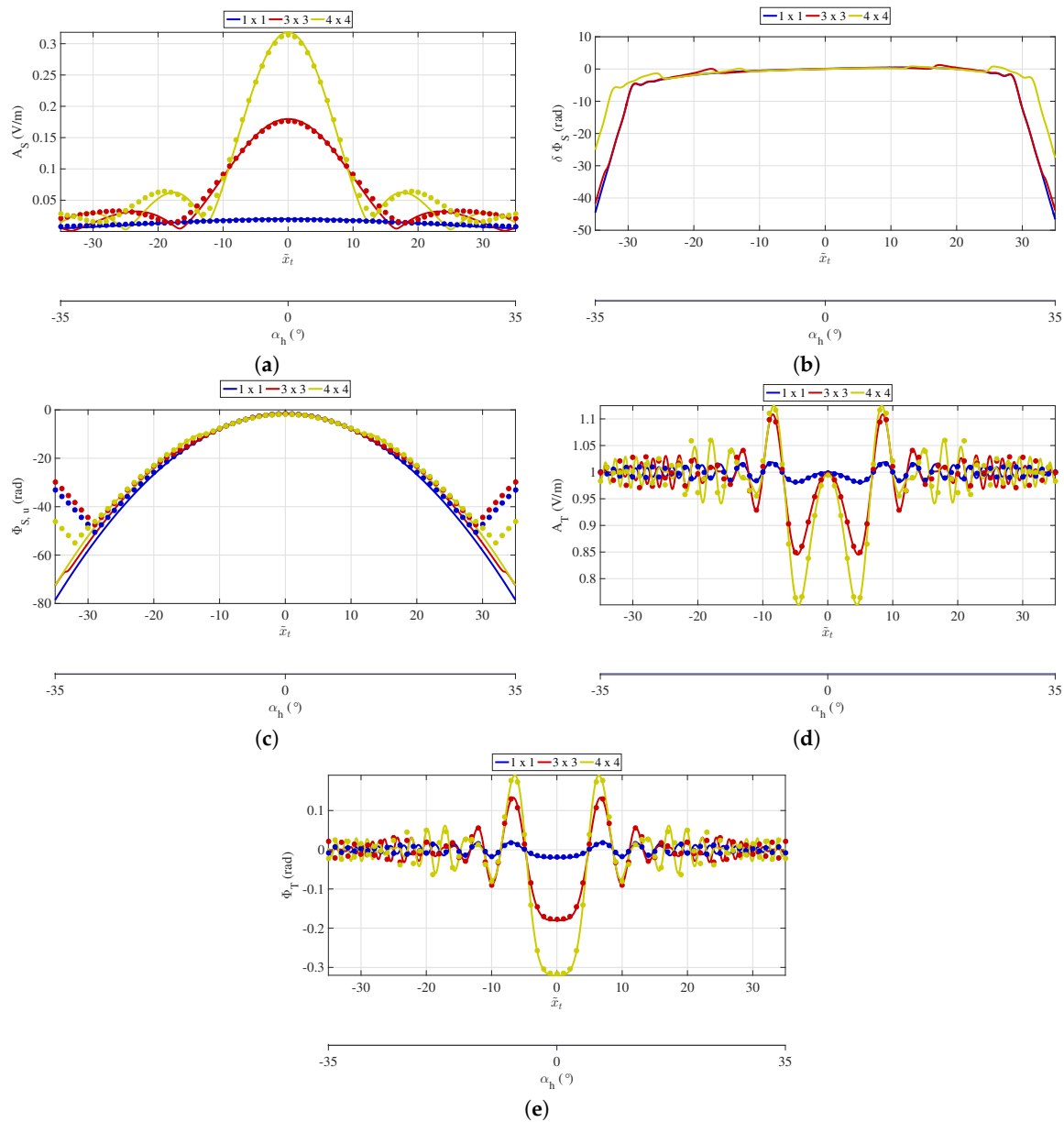
Figure 10. Scattered ('S') and total ('T') signals vs. target horizontal position, collected by the receiving antenna for three different square PEC objects as in Figure 9: Side 1 (blue), 3 (red), 4 (yellow). (**a**) Scattered-field amplitude; (**b**) scattered-field phase difference; (**c**) scattered-field unwrapped phase; (**d**) total-field amplitude; (**e**) total-field phase. Closed-form results (solid) and full-wave CAD (dots) are compared.
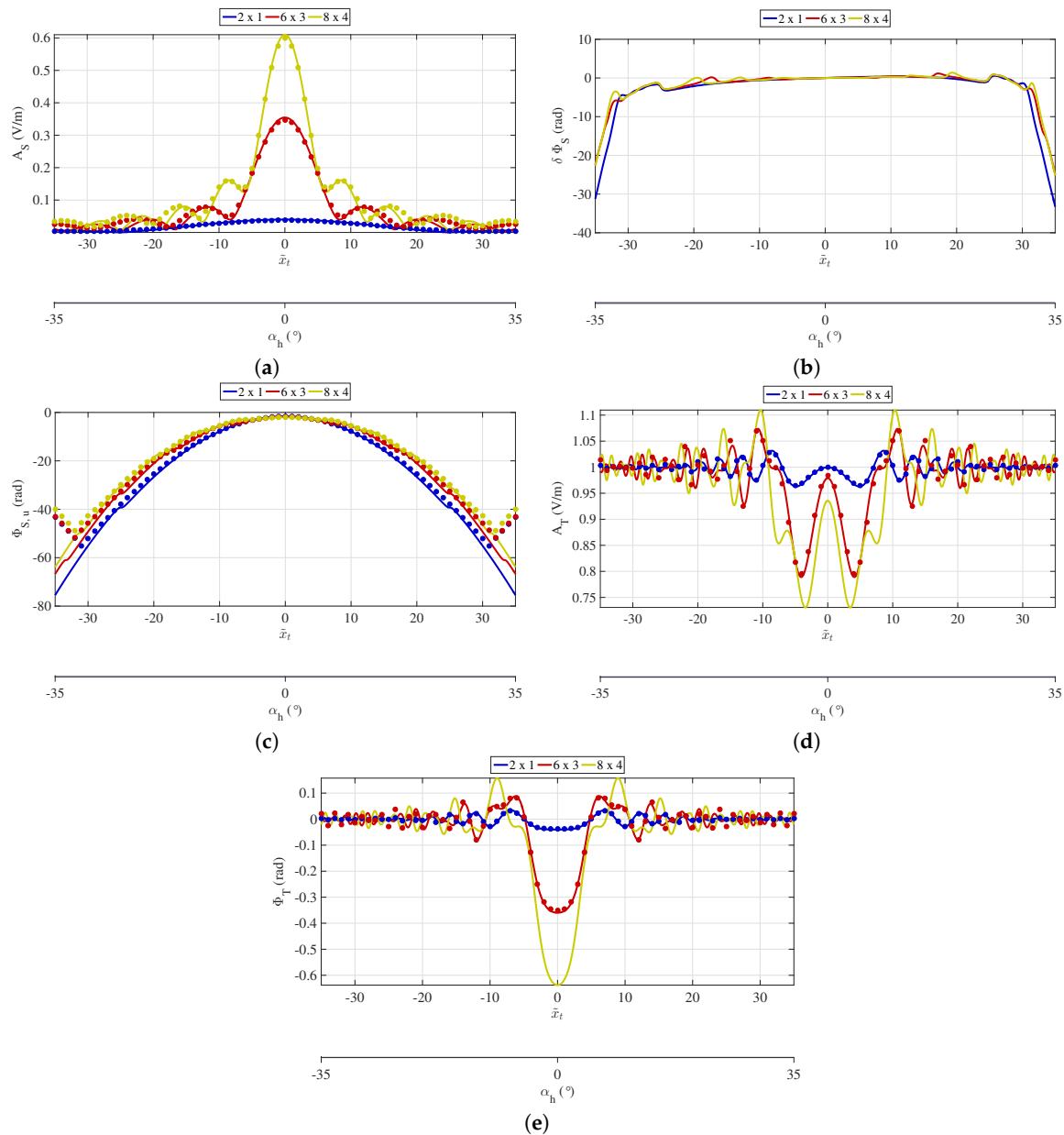
Figure 11. Same as of Figure 10 for various rectangular shapes, with $\tilde{b} = \tilde{a}/2 = 1$ (blue), 3 (red), 4 (yellow); see also Figure 9. (**a**) Scattered-field amplitude; (**b**) scattered-field phase difference; (**c**) scattered-field unwrapped phase; (**d**) total-field amplitude; (**e**) total-field phase. Closed-form results (solid) and full-wave CAD (dots) are compared.

Both the amplitude and phase of the scattered field mainly confirm the characteristics previously discussed. Differences on the re-irradiated field between the square and the rectangular shapes showing a common dimension for one of the two sides are anyway clearly visible. In both cases, as the object becomes larger, the field in the forward direction tends to be stronger and its distribution along the *x* axis narrower, whereas the phase distribution results in being less sensitive to the same variations. It is important to note that these results have been obtained by keeping fixed the Rx-antenna distance; hence, as expected, the effect generated by a larger object on the re-irradiated field is similar to that produced by a smaller object whose trajectory runs closer to the receiving antenna. In Figures 10c and 11c the unwrapped phase, along with the full-wave validation, is reported again for the square and rectangle, respectively, confirming the accuracy of the proposed formulation.

In Figures 10d,e and 11d,e, the amplitude and phase of the total field are displayed again for square and rectangular targets, respectively. Furthermore, in these cases, the amplitude of the total field oscillates around 1 V/m, and a fast variation is observed in the central part, for smaller objects. This is coherent with the strong variation observed in Figure 8d for the field re-irradiated when the same object is moving closer to the receiver. As concerns the phase, by increasing the target size, the chirp-like nature of the signal is progressively lost, since the presence of a larger object makes the apparent distance between the re-irradiating target and the Rx antenna smaller. It is still emphasized that there is an excellent agreement between closed-form (solid lines) and full-wave CAD results (dots).

4.3. Effect of the Trajectory

To analyze the effect of the trajectory, i.e., when a target is moving not necessarily perpendicular to the BL, in this subsection, different values of the ψ angle (see Figure 3) are considered. The distance from the receiver is set to $\tilde{z}_{Rx} = 100$ with respect to the central point (i.e., for $x = 0$), and the initial and final positions are $\tilde{x}_i = -90$ and $\tilde{x}_f = 90$. The moving object is a metallic square ($\tilde{a} = \tilde{b} = 3$), while all of the remaining parameters, included the impinging plane wave, are unchanged. Three different linear trajectories are considered at different tilt angles, i.e., $\psi_1 = 0°$, $\psi_2 = 30°$, $\psi_3 = 45°$; in order to evaluate the effect of each tilted trajectory, we keep fixed $\tilde{x}_i$ and $\tilde{x}_f$, so that the target could move along its path from the FF to NF regions. Consequently, three different asymmetric couples of angles of view are generated: the relevant geometrical details are reported in Table 2. Let us stress that, according to Figure 3, for $\psi > 0$, the moving object may result in the FF region for positive values of x and in the NF for those negative. Finally, it is important to note that, for modeling purposes, we considered here an object moving on a tilted trajectory, but showing always its flat face to the receiver; indeed, to consider an object whose profile is oriented along the direction of movement, one could refer to the shadow-contour theorem, whose validity along the transition between the FF-NF region deserves further investigation.

Table 2. Parameters of the trajectories.

$\psi(°)$	$\tilde{z}_{Rx}\vert_{\tilde{x}=0}$	$z_{Rx}\vert_{\tilde{x}=\tilde{x}_i}$	$\tilde{z}_{Rx}\vert_{\tilde{x}=\tilde{x}_f}$	$\alpha_{h,min}/\alpha_{h,max}(°)$
0	100	100	100	$-42/42$
30	100	50	160	$-62/31$
45	100	10	200	$-84/25$

For these results, we furnish again a comparison among our analytical model of Equation (10) ('AM', gray curves), the numerical model of Equation (7) ('NM', black curves) based on the computation of the diffraction integral and the full-wave ('FW', dotted green curves) CAD implementation.

In Figure 12a,b, the scattered field (amplitude and phase, respectively) for $\psi = 0°$ (straight trajectory, perpendicular to BL) is presented: with respect to the results reported in the previous sections in this case, we can test the effect of the paraxial approximation (fully satisfied for relatively small α_h) on the re-irradiated field. An excellent agreement is obtained in the central region for both amplitude and phase of the signal, whereas the agreement is gradually lost as x and consequently α_h increase. In Figure 12c–f, the amplitude and phase results of the scattered fields for the two tilted trajectories, ψ_2 and ψ_3, are presented: as expected, the amplitude of the scattered field loses its symmetry, and the agreement among the analytical model, the numerical solution of the integral and the full-wave validation is gradually lost along the path, i.e., in particular as the object approaches toward the negative values of x, entering NF regions.

In Figure 13, the same results of tilted trajectories are for the total field. Again, the symmetry is lost for $\psi \neq 0$, and the amplitude of the total field oscillates around 1 V/m; even though the typical chirp signature results in being perturbed, this behavior allows us to recognize a trajectory different from 0° and to potentially provide an estimation of the tilted angle. Once again, the results have been

validated by means of the full-wave CAD solution, and an excellent agreement has still been obtained as long as the paraxial approximation is satisfied.
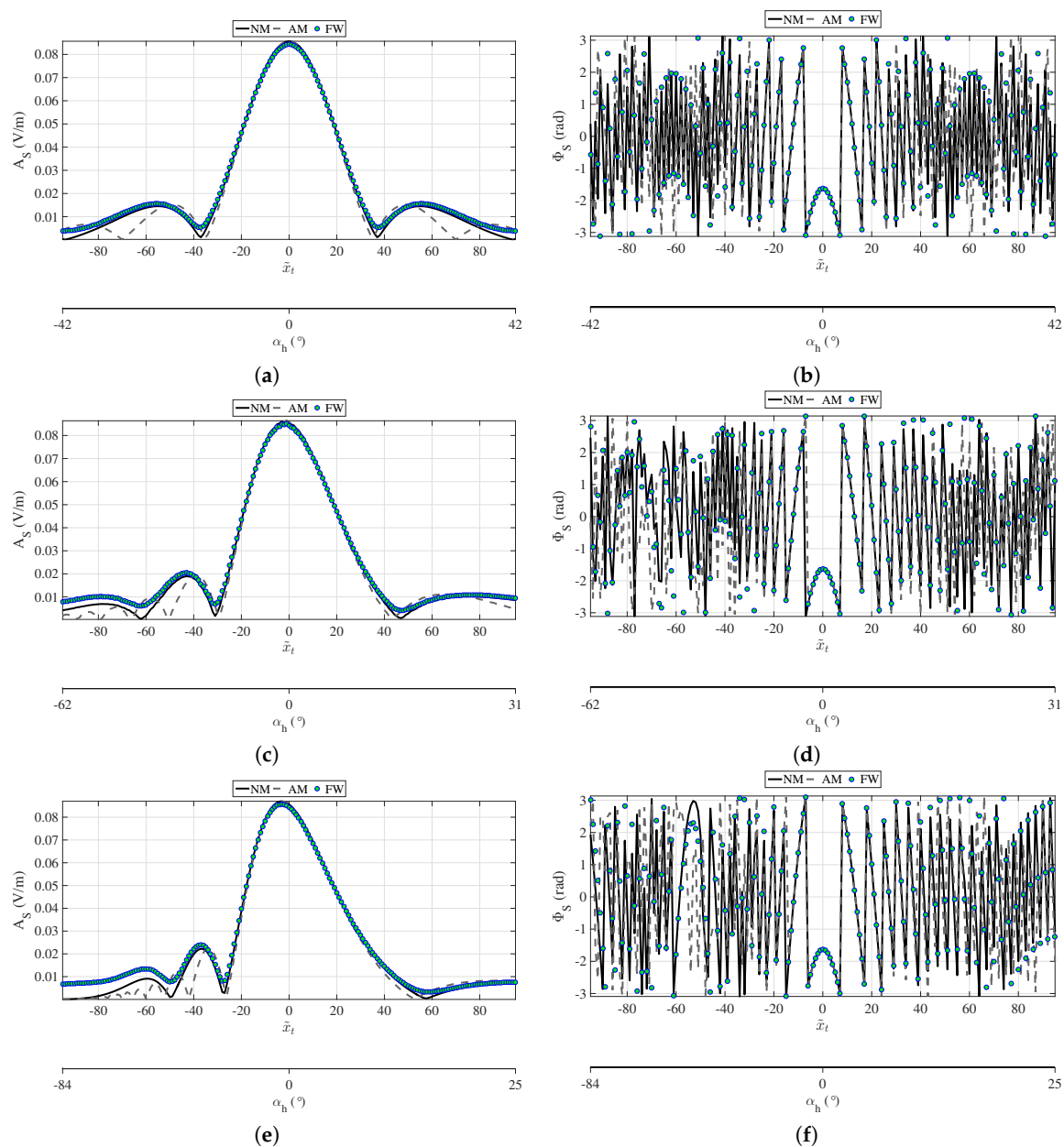
Figure 12. Amplitude (left column) and phase (right column) of the scattered field collected by the receiving antenna for different tilt angles ψ of the target trajectory (see Figure 3). Parameters: $\tilde{a} = \tilde{b} = 3$, frequency f. The EM field radiated by the source is still assumed as a z-directed plane wave polarized along the y-direction. Comparisons between analytical model (AM, gray curves), numerical model (NM, black curves) and full-wave (FW, green dots) CAD are displayed. Cases (**a**) and (**b**) for $\psi = 0°$; (**c**,**d**) for $\psi = 30°$; (**e**,**f**) for $\psi = 45°$.
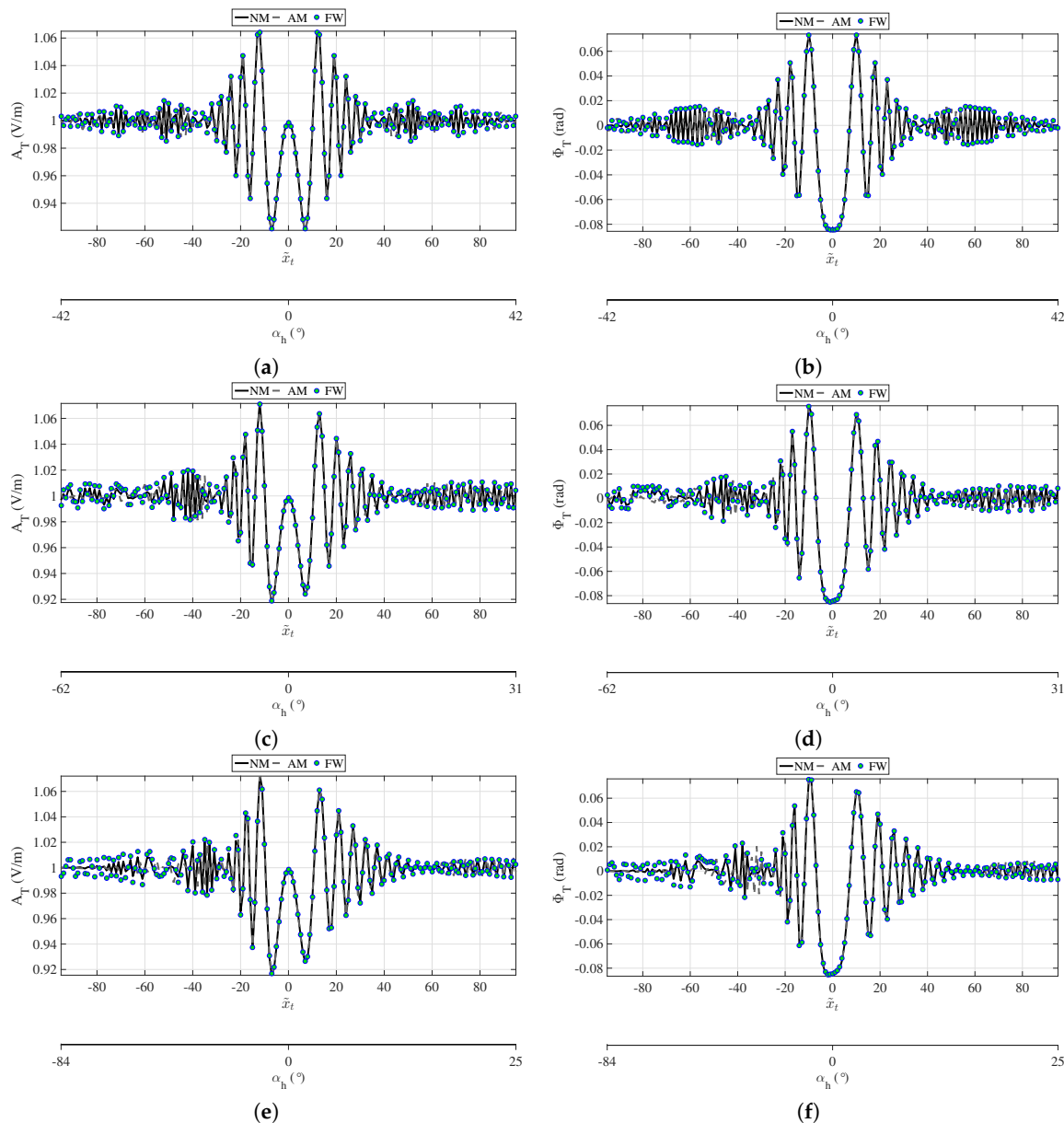
Figure 13. As in Figure 12 for the total field. (**a**,**b**) $\Psi = 0°$; (**c**,**d**) $\Psi = 30°$; (**e**,**f**) $\Psi = 45°$.

5. Conclusions

Since FSR systems are able to provide an enhanced detection capability that can be very effective for the monitoring of UAV and low-observable targets, a comprehensive electromagnetic model has been presented in this work for the characterization of the forward scattering generated by two-dimensional shapes, useful when the receiver is either in far-field and in near-field with respect to the target illuminated by a plane wave.

A simple but efficient closed-form expression has been derived and tested for canonical shapes by taking into account different target dimensions and trajectories. The validity of the proposed analytical approach has been discussed and confirmed through numerical evaluations of the scattering integrals and also by implementing an ad hoc full-wave solution with a commercial EM CAD tool for the same scenarios.

The results have emphasized to what extent the FF-NF transition is efficiently described by the closed-form model, so that it can be used to suitably investigate the fundamental characteristics of the FSR phenomenon in particularly critical applications.

This work can thus represent a basic step toward the design of a comprehensive model capable of better characterizing and describing an FSR operating in challenging realistic conditions. Consequently, useful guidelines can be outlined for the design of optimal signal processing techniques of FSR systems. Additional developments may be focused on systematic parametric analyses of the FSR signatures including the study of wider classes of targets, made of different materials (e.g., dielectric) and having various shapes for both 2D and 3D geometries.

Author Contributions: A.G., P.L., and F.S.M. conceived and designed the experiments; M.T.F. and D.C. performed the experiments; M.T.F., D.C., A.G., D.P., P.L., and F.S.M. analyzed the data; A.G., P.L., and F.S.M. contributed materials and analysis tools; M.T.F. and D.C. wrote the paper.

Conflicts of Interest: The authors declare no conflict of interest.

Abbreviations

The following abbreviations are used in this manuscript:

BL	baseline
BP	Babinet's principle
CAD	computer-aided design
CW	continuous wave
EM	electromagnetic
FF	far-field
FS	forward scattering
FS-CS	forward-scatter cross-section
FSR	forward scatter radar
NF	near-field
PEC/PMC	perfect electric conductor/perfect magnetic conductor
PO	physical optics
PTD	physical theory of diffraction
RCS	radar cross-section
TEM	transverse electromagnetic
Tx/Rx	transmitting/receiving
UAV	unmanned aerial vehicle

Appendix A. Analytical Formula for EM Model

We focus here on the mathematical steps that lead to the analytical expression of the EM model in Equation (12). Recalling the generalized expression in Equation (10):

$$E_T^{pl}(\tilde{\mathbf{r}}) \quad = E_0 \left(e^{-j\tilde{k}\tilde{z}_{Rx}} - \frac{1}{2\pi} \int_{\tilde{A}} \left(j\tilde{k} + \frac{1}{\tilde{R}} \right) \frac{\tilde{z}_{Rx}}{\tilde{R}^2} e^{-j\tilde{k}\tilde{R}} \, d\tilde{A}' \right) \tag{A1}$$

we follow the (i) and (ii) approximations in Section 3.2 by replacing the distance $\tilde{R}$ with Equation (11) and then Equation (10):

$$E_T^{pl}(\tilde{\mathbf{r}}) \quad = E_0 e^{-j\tilde{k}\tilde{z}_{Rx}} \left(1 - \frac{1}{2\pi} \left(j\tilde{k} + \frac{1}{\tilde{R}_0} \right) \frac{\tilde{z}_{Rx}}{\tilde{R}_0^2} \int_{\tilde{A}} e^{-j\tilde{k}\frac{(\tilde{x}_t-\tilde{x}')^2+(\tilde{y}_t-\tilde{y}')^2}{2\tilde{z}_{Rx}}} \, d\tilde{x}'d\tilde{y}' \right) \tag{A2}$$

Now, we consider the integral:

$$\int_{\tilde{A}} e^{-j\tilde{k}\frac{(\tilde{x}_t-\tilde{x}')^2+(\tilde{y}_t-\tilde{y}')^2}{2\tilde{z}_{Rx}}} \, d\tilde{x}'d\tilde{y}' =$$

$$\left[-\int_0^{-\tilde{a}/2} e^{-j\tilde{k}\frac{(\tilde{x}_t-\tilde{x}')^2}{2\tilde{z}_{Rx}}} \, d\tilde{x}' + \int_0^{\tilde{a}/2} e^{-j\tilde{k}\frac{(\tilde{x}_t-\tilde{x}')^2}{2\tilde{z}_{Rx}}} \, d\tilde{x}' \right] \left[-\int_0^{-\tilde{b}/2} e^{-j\tilde{k}\frac{(\tilde{y}_t-\tilde{y}')^2}{2\tilde{z}_{Rx}}} \, d\tilde{y}' + \int_0^{\tilde{b}/2} e^{-j\tilde{k}\frac{(\tilde{y}_t-\tilde{y}')^2}{2\tilde{z}_{Rx}}} \, d\tilde{y}' \right] = \tag{A3}$$

$$\frac{\tilde{z}_{Rx}}{2}[-C(p^-) + jS(p^-) + C(p^+) - jS(p^+)][-C(q^-) + jS(q^-) + C(q^+) - jS(q^+)]$$

The last expression derives from the definition of Fresnel integrals $\int_0^z exp(-j(\pi/2)t^2)\,dt = C(z) - jS(z)$ [27] and leads directly to the EM formulation in Equation (12). Similar mathematical steps have been applied to the expression valid only in the far-field (Fraunhofer) condition of Equation (16).

References

1. Blyakhman, A.B.; Burov, V.N.; Myakinkov, A.V.; Ryndyk, A.G. Detection of unmanned aerial vehicles via multi-static forward scattering radar with airborne transmit positions. In Proceedings of the 2014 International Radar Conference (Radar), Lille, France, 13–17 October 2014; pp. 1–5.

2. Fadeev, R.S.; Myakinkov, A.V.; Ryndyk, A.G.; Ogurtsov, A.G. Detection and tracking of low-observable targets via multi-static forward scatter radar with airborne positions. In Proceedings of the 2015 16th International Radar Symposium (IRS), Dresden, Germany, 24–26 June 2015; pp. 242–247.

3. Willis, N.; Griffiths, H. *Advances in Bistatic Radar*; Institution of Engineering and Technology: Stevenage, UK, 2007.

4. Glaser, J.I. Fifty years of bistatic and multistatic radar. *IEE Proc. F Commun. Radar Signal Proc.* **1986**, *133*, 596–603.

5. Glaser, J.I. Bistatic RCS of complex objects near Forward Scatter. *IEEE Trans. Aerosp. Electron. Syst.* **1985**, *21*, 70–78.

6. Ufimtsev, P.Y. Diffraction of electromagnetic waves at blackbodies and semitransparent plates. *Radiophys. Quantum Electron.* **1968**, *11*, 527–538.

7. Ufimtsev, P.Y. New insight into the classical Macdonald physical optics approximation. *IEEE Trans. Antennas Propag.* **2008**, *50*, 11–20.

8. Boyle, R.J.; Wasylkiwskyj, W. Comparison of monostatic and bistatic bearing estimation performance for low RCS targets. *IEEE Trans. Aerosp. Electron. Syst.* **1994**, *30*, 962–968.

9. Suberviola, I.; Mayordomo, I.; Mendizabal, J. Experimental results of air target detection with a GPS forward-scattering radar. *IEEE Geosci. Remote Sens. Lett.* **2012**, *9*, 47–51.

10. Kabakchiev, C.; Garvanov, I.; Behar, V.; Rohling, H. The experimental study of possibility for radar target detection in FSR using L1-based non-cooperative transmitter. In Proceedings of the 2013 14th International Radar Symposium (IRS), Dresden, Germany, 19–21 June 2013; pp. 625–630.

11. Kabakchiev, C.; Garvanov, I.; Behar, V.; Daskalov, P.; Rohling, H. Study of moving target shadows using passive Forward Scatter radar systems. In Proceedings of the 2014 15th International Radar Symposium (IRS), Gdansk, Poland, 16–18 June 2014; pp. 1–4.

12. Marra, M.; Luca, A.D.; Hristov, S.; Daniel, L.; Gashinova, M.; Cherniakov, M. New algorithm for signal detection in passive FSR. In Proceedings of the 2015 IEEE Radar Conference, Johannesburg, South Africa, 27–30 October 2015; pp. 218–223.

13. Kabakchiev, C.; Garvanov, I.; Behar, V.; Kabakchieva, D.; Kabakchiev, K.; Rohling, H.; Kulpa, K.; Yarovoy, A. The study of target shadows using passive FSR systems. In Proceedings of the 2015 16th International Radar Symposium (IRS), Dresden, Germany, 24–26 June 2015; pp. 628–633.

14. Abdullah, R.S.A.R.; Salah, A.A.; Aziz, N.H.A.; Rasid, N.E.A. Vehicle recognition analysis in LTE based forward scattering radar. In Proceedings of the 2016 IEEE Radar Conference (RadarConf), Philadelphia, PA, USA, 2–6 May 2016; pp. 1–5.

15. Martelli, T.; Colone, F.; Lombardo, P. First experimental results for a WiFi-based passive forward scatter radar. In Proceedings of the 2016 IEEE Radar Conference (RadarConf), Philadelphia, PA, USA, 2–6 May 2016; pp. 1–6.

16. Blyakhman, A.B.; Runova, I.A. Forward scattering radiolocation bistatic RCS and target detection. In Proceedings of the Record of the 1999 IEEE Radar Conference, Waltham, MA, USA, 22–22 April 1999; pp. 203–208.

17. Gashinova, M.; Daniel, L.; Sizov, V.; Hoare, E.; Cherniakov, M. Phenomenology of Doppler forward scatter radar for surface targets observation. *IET Radar Sonar Navig.* **2013**, *7*, 422–432.

18. Zeng, T.; Li, X.; Hu, C.; Long, T. Investigation on accurate signal modelling and imaging of the moving target in ground-based forward scatter radar. *IET Radar Sonar Navig.* **2011**, *5*, 862–870.

19. Gashinova, M.; Daniel, L.; Cherniakov, M.; Lombardo, P.; Pastina, D.; Luca, A.D. Multistatic Forward Scatter Radar for accurate motion parameters estimation of low-observable targets. In Proceedings of the 2014 International Radar Conference, Lille, France, 13–17 October 2014; pp. 1–4.

20. Contu, M.; Pastina, D.; Lombardo, P.; Luca, A.D.; Gashinova, M.; Daniel, L.; Cherniakov, M. Target motion estimation via multistatic Forward Scatter Radar. In Proceedings of the 2015 16th International Radar Symposium (IRS), Dresden, Germany, 24–26 June 2015; pp. 616–621.

21. Pastina, D.; Contu, M.; Lombardo, P.; Gashinova, M.; Luca, A.D.; Daniel, L.; Cherniakov, M. Target motion estimation via multi-node forward scatter radar system. *IET Radar Sonar Navig.* **2016**, *10*, 3–14.

22. Ustalli, N.; Pastina, D.; Lombardo, P. Theoretical performance prediction for the detection of moving targets with Forward Scatter Radar systems. In Proceedings of the 2016 17th International Radar Symposium (IRS), Krakow, Poland, 10–12 May 2016.

23. Falconi, M.T.; Comite, D.; Galli, A.; Lombardo, P.; Marzano, F.S. Forward scatter radar modeling: Effects of near field for canonical targets. In Proceedings of the 2015 IEEE International Symposium on Antennas and Propagation USNC/URSI National Radio Science Meeting, Vancouver, BC, Canada, 19–24 July 2015; pp. 492–493.

24. Falconi, M.T.; Comite, D.; Marzano, F.S.; Galli, A.; Lombardo, P. Analysis of canonical targets in near field for Forward Scatter Radar applications. In Proceedings of the 2015 European Radar Conference (EuRAD), Paris, France, 9–11 September 2015; pp. 77–80.

25. Hu, C.; Sizov, V.; Antoniou, M.; Gashinova, M.; Cherniakov, M. Optimal signal processing in ground-based forward scatter micro radars. *IEEE Trans. Aerosp. Electron. Syst.* **2012**, *48*, 3006–3026.

26. Ufimtsev, P.Y. *Fundamentals of the Physical Theory of Diffraction*; Wiley and Sons: Hoboken, NJ, USA, 2007.

27. Ishimaru, A. *Electromagnetic Wave Propagation, Radiation, and Scattering*; Prentice Hall: Upper Saddle River, NJ, USA, 1991.

28. Balanis, C.A. *Antenna Theory: Analysis and Design*, 3rd ed.; Wiley and Sons: Hoboken, NJ, USA, 2005.

29. Kubicke, G.; Yahia, Y.A.; Bourlier, C.; Pinel, N.; Pouliguen, P. Bridging the gap between the Babinet principle and the physical optics approximation: Scalar problem. *IEEE Trans. Antennas Propag.* **2011**, *59*, 4725–4732.

30. Shavit, R.; Cohen, A.; Ngai, E.C. Characterization of forward scattering parameters from an arbitrarily shaped cylinder by near-field probing. *IEEE Trans. Antennas Propag.* **1995**, *43*, 585–590.

31. Gould, D.M.; Orton, R.S.; Pollard, R.J.E. Forward scatter radar detection. In Proceedings of the RADAR 2002, Edinburgh, UK, 15–17 October 2002; pp. 36–40.

32. Changjiang, L.; Cheng, H.; Jia, X.; Teng, L. Modified signal modeling and imaging method of non-perpendicular crossing targets in forward scatter radar. In Proceedings of the 2014 IEEE Radar Conference, Lille, France, 13–17 October 2014; pp. 291–295.

33. Rashid, N.E.A.; Gashinova, M.; Sizov, V.; Cherniakov, M.; Ismail, N.N. The influence of different baseline lengths to ground target signature in a FS micro-radar network. In Proceedings of the 2013 IEEE 9th International Colloquium on Signal Processing and Its Applications (CSPA), Kuala Lumpur, Malaysia, 8–10 March 2013; pp. 21–26.

34. Hu, C.; Liu, C.; Wang, R.; Zeng, T. Improved reconstruction of radio holographic signal for Forward Scatter Radar Imaging. *Sensors* **2016**, *16*, 651.

35. Mei, K.; Bladel, J.V. Scattering by perfectly-conducting rectangular cylinders. *IEEE Trans. Antennas Propag.* **1963**, *11*, 185–192.

36. FEKO. 2015. Available online: https://www.feko.info/ (accessed on 13 February 2016).